ELSEVIER

Contents lists available at ScienceDirect

Materials Today Communications

journal homepage: www.elsevier.com/locate/mtcomm





The quest for optimal photovoltaics: A theoretical exploration of quasi-one-dimensional tin based chalcogenides XSnS₃ (X=Ba, Sr)

Chethan V. a, Sujith C.P. b, Thomas Mathew c, Mahendra M. a,*

- ^a Department of Studies in Physics, University of Mysore, Manasagangotri, Mysuru 570 006, Karnataka, India
- ^b PG Department of Physics, JSS College of Arts, Commerce, and Science, Ooty Road Mysuru 570 004, Karnataka, India
- ^c Department of Physics, St Stephen's College, Uzhavoor, Kerala, India

ARTICLE INFO

Keywords: Quasi-one-dimensional Mechanical properties Structural and electronic properties Optical anisotropy Density functional theory (DFT)

ABSTRACT

Structural, mechanical, electronic, and optical properties of alkaline metals (Ba, Sr) tin chalcogenide were investigated by the first principles method based on density functional theory (DFT) implemented in the WEIN2K program. The study found that both materials exhibit a quasi-one-dimensional nature along the b-axis, and the optimized structure agrees with the available experimental data. Mechanical properties revealed that both materials are mechanically stable, exhibit ductility, and have significant anisotropy. BaSnS $_3$ and SrSnS $_3$ exhibit an indirect band gap with the values of 1.55 eV and 1.39 eV, respectively. Which is favorable for photovoltaic solar cell absorber materials. Like many ternary metal chalcogenides, XSnS $_3$ compounds show significant anisotropy in the optical properties due to their quasi-one-dimensional structure. This work determined the degree of optical anisotropy of XSnS $_3$ in terms of the dielectric function, refractive index, optical absorption, reflectivity, optical extinction, birefringence, and energy loss function. The results indicate that BaSnS $_3$ and SrSnS $_3$ materials possess notable optical anisotropy and a high absorption coefficient ($\alpha \approx 10^6 \text{ cm}^{-1}$), low reflectivity and energy loss function within the visible and ultraviolet energy range. It indicates their potential for use in a range of applications, such as sensors, optoelectronics, and photovoltaic solar cell absorber materials.

1. Introduction

Mixed organic-inorganic halide perovskites represent a notable breakthrough in photovoltaic (PV) materials. Within a decade, their utilization in PV devices has dramatically improved the power conversion efficiency (PCE) from 3.8% to an impressive 24.2% [1,2]. However, these materials suffer from instability and toxicity issues due to lead (Pb) [3]. To overcome these challenges, exploring alternative semiconductor compounds that possess the desired characteristics for PV applications is intriguing, including an optimal band gap within the range of 0.5 to 2.5 eV, high carrier mobility, and a stable crystal structure [1]. Metal halide perovskites have indeed received significant attention from the scientific community [4]. A recent study by S. Idrissi et al. [5] indicated that CsXCl₃ (X = Ge, Sn, and Pb) halide perovskites have good photovoltaic properties due to their desirable band gaps. Furthermore, Cs-based fluoro-perovskites such as CsMF₃ (M = Ge, Sn, and Pb) have demonstrated promising thermoelectric and optoelectronic properties [6]. The photovoltaic community has been looking for lead-free perovskites [7] and organic-inorganic materials for photovoltaic applications for several years. Recent studies revealed

that Sn substitution in methyl ammonium lead halide decreases toxicity and is suitable for optimum solar cell efficiency [8].

BaSnS3 and SrSnS3 materials are ternary chalcogenide materials that crystallize in an orthorhombic D_{2h}-Pnma space group, forming a needle-like structure isostructural to NH₄CdCl₃. The quasi-onedimensional nature of these materials is observed along the b-axis of the unit cell, which indicates strong anisotropy of the structural and physical properties of the materials [9,10]. Sujith et al. [11] observed anisotropy in HfSnS3 and ZrSnS3 ternary chalcogenide materials. They found that both materials display substantial birefringence with quite sizeable optical anisotropy and can potentially be employed as photovoltaic absorber materials. Yang Lu et al. [12] recently synthesized HfSnS3 and confirmed that it forms a one-dimensional Van der Walls P-type semiconducting material. This material exhibits giant anisotropy and substantial photo response in a broadband range from UV to near-infrared (NIR) with short response times of 0.355 ms, high responsivity of 11.5 AW⁻¹, detectivity of 8.2×10^{11} Jones, and environmental stability, making it suitable for photodetector and opto-electronic applications.

E-mail address: mahendra@physics.uni-mysore.ac.in (Mahendra M.).

^{*} Corresponding author.

 $XSnS_3$ (X = Ba, Sr) materials are quasi-one-dimensional (Q1D) chalcogenides with a favorable band gap for solar cell application. The desirable band gap makes them promising materials for photovoltaic absorber material [13,14]. It motivates us to study other physical properties to understand the suitability of these materials for optoelectronic and photonics applications. Earth-abundant Ba, Sr, Sn, and S atoms in XSnS₃ materials make it low-cost, non-toxic, and favorable for manufacturing. A recent study signifies that both materials have good thermoelectric properties and can be high-performance thermoelectric materials [15]. S. Yamaoka and B. Okai [16] first synthesized tin sulfides BaSnS3, SrSnS3, and PbSnS3 by an equimolar mixture of AS (A = Ba, Sr, and Pb) and SnS₂ using high-pressure apparatus at 500 to 800 °C and 20 kbar, none of them exhibited perovskite structural transformation. They also suggested that it will not form perovskite structures below 60 kbar and 900 °C. Later, Bin Okai [17] confirmed that both BaSnS₃ and SrSnS₃ possess isostructural with NH₄CdCl₃ at 60 kbar and 800 °C and could not form perovskite structures.

The present work investigated the structural, mechanical, electronic, and optical characteristics of the titled materials using DFT with different approximations and compared the results with previously available experimental and computational data. While the structural properties of these materials are known through various experimental studies, the anisotropic behavior of elastic properties and optical properties such as the dielectric function, absorption coefficient, refractive index, birefringence, and dichroism of XSnS3 materials have not yet been explored in both experimentally and theoretically, which makes theoretical predictions necessary. The structural optimization in this work is done with the GGA-PBE functional, and the optimized lattice parameters agree well with the available experimental results. Mechanical properties such as Young's modulus, Poisson's ratio, Shear modulus, and so on are explored using the Irelast package as implemented in the WIEN2K program, and the results demonstrate that both materials are mechanically stable, ductile, and have significant anisotropy. Electronic properties have been studied using TB-mBJ functional, one of the most reliable methods for predicting electronic structure calculation. The obtained band gaps are compared with available reports. We have incorporated spin-orbit coupling, which plays a significant role in obtaining the electronic band gap of heavy elements such as Pb, Bi, etc. [18-20], and found that the spin orbit coupling (SOC) effect is negligible for both BaSnS3 and SrSnS3 materials. A material's optical anisotropy can be estimated by computing characteristics like birefringence, dielectric function, etc. According to a recent study, quasi-one-dimensional barium titanium chalcogenides based on barium exhibit large optical anisotropy with broadband giant birefringence over the infrared region [21,22]. Optically anisotropic materials have potential use in optical communication, laser manufacturing, polarimetry, and photovoltaics [23].

2. Computational methods

The ab initio computations were carried out using the FP-LAPW (Full Potential Linear Augmented Wave) method employed in the WIEN2k code [24,25]. In all our studies, self-consistent calculations were performed to solve the Kohn-Sham equations [26] incorporating the Generalized Gradient Approximation and Perdew-Burke-Ernzerhof (GGA-PBE) [27] as the exchange-correlation functional. The structural optimization is carried out using GGA-PBE functional with Van der Waals corrections. Until the Hellmann-Feynman forces were less than 10⁻³ Ry/a.u. and energy convergence criteria of 10⁻⁶ Ry to obtain the equilibrium structure. Many precise plane waves (PWs) have been used to ensure accurate calculations. It is achieved by setting $R_{MT} \times K_{max}$ = 7. Here, K_{max} denotes the largest reciprocal lattice vector employed in the expansion of plane waves, while R_{MT} represents the minimum radius of the smallest muffin-tin (MT) sphere. The Brillouin zone was integrated at 1000 k-points for both the material with $9 \times 20 \times 5$ for $BaSnS_3$ and $9 \times 19 \times 5$ for $SrSnS_3$, respectively. TB-mBJ [28] method

Table 1

Lattice parameters, atomic coordinates and Wyckoff positions of XSnS₃ structures.

Lattice constants given in brackets are experimental data.

	,							
BaSnS_3					SrSnS	3		
Lattice constants	c = 1		14.69	Å [16] Å [16] Å [16] 6 Å ³ [16]		.91 Å 4.30 Å		
Atomic coordina	tes and	Wyckoff	positio	ns (WP)				
Atom	x	у	z	WP	х	у	z	WP
X	0.076	0.75	0.826	4c	0.078	0.75	0.823	4c
Sn	0.167	0.25	0.556	4c	0.172	0.25	0.558	4c
S1	0.027	0.25	0.400	4c	0.027	0.25	0.394	4c
S2	0.163	0.25	0.997	4c	0.150	0.25	0.995	4c
S3	0.212	0.75	0.207	4c	0.201	0.75	0.215	4c

Table 2
Sn coordination in XSnS₃: bond length and bond angles.

Bond	Bond length (Å)				
	BaSnS ₃	SrSnS ₃			
Sn-S1	2.689	2.660			
Sn-S2	2.624	2.614			
Sn-S1(b)	2.609	2.635			
Sn-S3	2.470	2.484			
Angles (°)	BaSnS ₃	SrSnS ₃			
S2-Sn-S1	82.374	83.666			
S2-Sn-S3	93.695	94.036			
S1-Sn-S2	88.065	87.442			
S2-Sn-S2	98.853	97.096			
S1-Sn-S1	95.662	94.870			

⁽b) Represents the S1 atom positioned at the bottom of the octahedron.

is used to elucidate the electrical and optical properties of the material incorporating spin orbit coupling (SOC), and Grimme's DFT-D3 method by Becke–Jonson damping was used to introduce Van der Waals corrections. The elastic constants that determine the mechanical properties of the materials are computed using the IRelast [29] package.

3. Results and discussion

3.1. Structural properties

The crystal structures of the XSnS₃ (X = Ba, Sr) class of materials were investigated using X-ray diffraction data, confirming their orthorhombic D_{2h}^{16} -Pnma space group [16]. The materials XSnS₃ are isostructural with PbZrS₃ [30], SnHfS₃, PbHfS₃ [31], NH₄CdCl₃ [32,33] and MSnS₃ (M = Zr, Hf) [11]. In this work, structural optimization of XSnS₃ compounds has been carried out using the GGA-PBE method. Since the compounds are known to possess a quasi-one-dimensional structure, we incorporated Van der Waals corrections during the structural optimization using Grimme's DFT-D3 method with Becke-Jonson damping functions. The optimized lattice parameters, atomic coordinates, and Wyckoff positions are listed in Table 1. Both XSnS₃ materials form four formula units in their unit cells, as shown in Fig. 1. The coordination of both materials appears to be similar, as they both crystallize in the orthorhombic space group D_{2h}^{16} -pnma. The findings of structural calculations agree well with the existing experimental data [16]. Upon observation, it is apparent that the lattice constants and cell volume of BaSnS₃ are larger than those of SrSnS₃. This difference can be attributed to the larger size of the Ba^{2+} ion [34].

Figs. 2(d) and 2(e) depicts quasi-one-dimensional chains of edgesharing SnS_6 octahedra, which extend parallel to the *b*-axis in the perspective view of $BaSnS_3$ and $SrSnS_3$ unit cell, respectively. The gap between these chains is occupied by a pair of Ba^{2+}/Sr^{2+} cations coordinated with eight S^{2-} anions. This coordination results in a bicapped

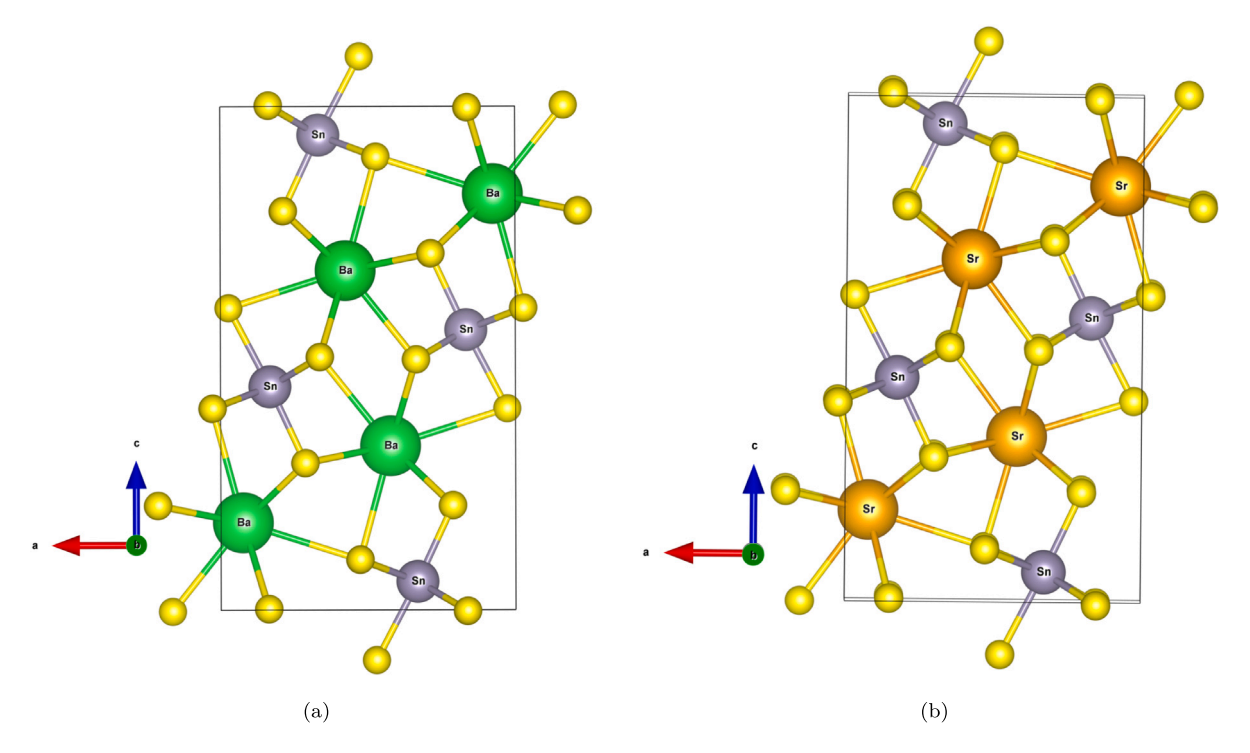


Fig. 1. Crystal structure of (a) BaSnS₃ and (b) SrSnS₃ in a unit cell, each containing four formula units. Presented with Ba–green, Sr–orange, Sn–gray, and S–yellow spheres respectively. (For interpretation of the references to color in this figure legend, the reader is referred to the web version of this article.)

Table 3 X-S (X = Ba, Sr) coordination in $XSnS_3$: bond length and bond angles.

Bond	Bond length (Å)				
	BaSnS ₃	SrSnS ₃			
X-S3	3.134	3.204			
X-S3 ^(r)	3.240	3.099			
X-S2	3.220	3.100			
X-S1 ^(cap)	3.334	3.218			
X-S2 ^(cap)	3.467	3.243			
Angles (°)	BaSnS ₃	SrSnS ₃			
S3-X-S3	73.963	75.392			
$S3^{(r)}$ -X- $S3^{(r)}$	75.914	78.409			
S2-X-S2	76.460	78.389			
S1-X-S3	62.771	59.633			
S1-X-S3 ^(r)	68.866	72.359			

⁽cap) Represents the anion capping the bicapped trigonal pyramidal structure.

trigonal prismatic geometry with a rectangular face capped by two S^{2-} ions, as shown in Fig. 2(a).

A distorted octahedron (SnS $_6$) forms when a Sn is coordinated with six S atoms, as shown in Fig. 2(b). These SnS $_6$ octahedra share their edges, resulting in an infinite chain of units along the b-axis and a quasi-one-dimensional structure. The octahedra mainly coordinated with three inequivalent S 2 - anions, namely, S1, S2, and S3, with their bond lengths and angles as shown in Fig. 2(b). The detailed bond lengths and angles of the distorted SnS $_6$ octahedra are listed in Table 2. For instance, Sn-S1 and Sn-S3 form two bonds, each with identical bond lengths on opposite sides of the octahedra with bond lengths of 2.689 Å, 2.624 Å for BaSnS $_3$ and 2.660 Å, 2.614 Å for SrSnS $_3$, respectively. Moreover, the upper and lower halves of the octahedra are bonded to two distinct S 2 - anions, S3 and S1. 2(c) illustrates edge-sharing octahedra with Sn–Sn bond lengths of 3.893 Å and 3.867 Å for BaSnS $_3$ and SrSnS $_3$, respectively.

Each X (Ba, Sr) atom is surrounded by eight sulfur atoms, forming a bicapped trigonal pyramidal structure. Fig. 2(a) shows BaS_8 geometry.

The optimized value of bond length for Ba-S is 3.60 Å, and for Sr-S, it is slightly shorter at 3.452 Å. It may be due to the larger ionic radius of the Ba²⁺ ion when compared to the Sr²⁺ ion. The coordination arrangement varies depending on the X-S bond length. If the bond length slightly decreases from the optimized value, the coordination changes to XS₇, which exhibits a monocapped trigonal prismatic geometry. This occurs when the X-S bond length is less than 3.47 Å for BaSnS₃ and 3.243 Å for SrSnS₃. On the other hand, a slight increase in the bond length results in the XSq coordination, representing a tricapped trigonal prismatic geometry for both materials. Fig. 2(a) depicts the bicapped trigonal pyramidal structure of BaS8, formed by the eight nearest Sulfur atoms. These atoms arrange themselves on a rectangular plane comprising two distinct S3 and S2 atoms, shown with length of 3.986 Å for S2-S2 and 4.420 Å for S2-S3, respectively. On the top side of the rectangular plane are coordinated with four equivalent S3 atoms. While on the bottom side is coordinated with two equivalent S2 atoms with a bond length of 3.134 Å. The two capped structure are coordinated by S1 and S2 on top and rear side of the rectangular plane. A similar type of coordination environment is observed for the SrS₈ structure, and detailed information concerned with the bond lengths and angles of the XS₈ coordination is given in Table 3. Notably, both capped atoms, Ba-S2 and Ba-S1, have extensive bond lengths of 3.467 Å and 3.334 Å, respectively.

3.2. Mechanical properties

The elastic characteristics of the materials can be used to predict the crystal's response to applied forces. Furthermore, these qualities aid in understanding the mechanical behavior of the compound. As a result, we used the elastic constants C_{ij} to calculate the materials's elastic characteristics and mechanical behavior. For an orthorhombic crystal, the elastic constants are reduced to nine different components [35], as listed in Table 4. The mechanical stability of a material is an important parameter to consider when evaluating its mechanical behavior. To assess mechanical stability, we utilize the Born stability criteria from Eq. (1). The conditions presented in the below equation are not all linear, instead they are polynomial functions of the elastic constants;

⁽r) Represents the S3 atoms located on the rear side of the rectangular plane.

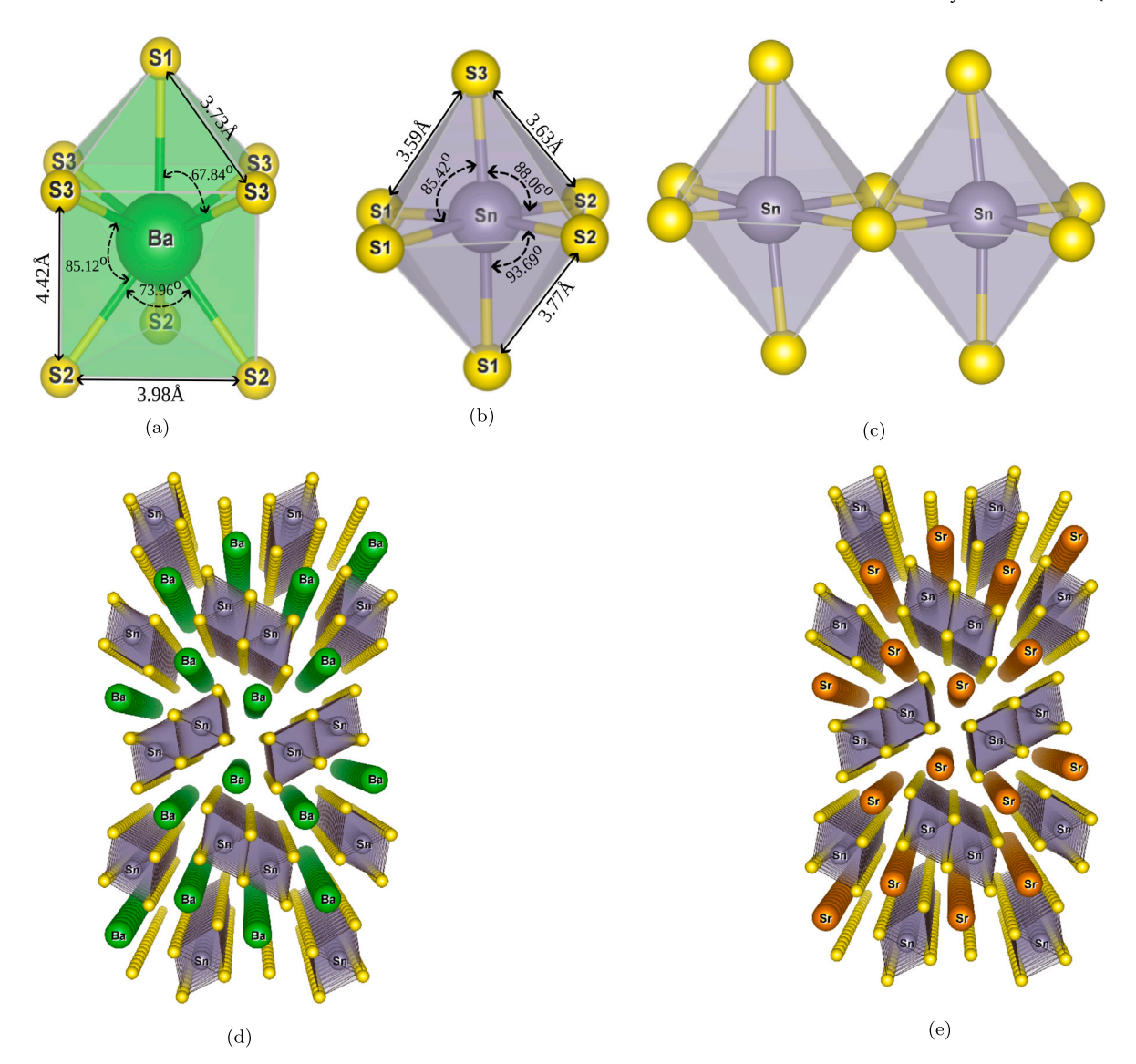


Fig. 2. Representation of local coordination environment for $BaSnS_3$: (a) Coordination of Ba with S anions forming bicapped trigonal prismatic (BaS_8) geometry, (b) S anions with S anions form edge sharing SnS_6 octahedron, (c) the edge-sharing octahedra. Quasi-one-dimensional perspective view of bulk (d) $BaSnS_3$ and (e) SnS_3 materials.

because the largest non-diagonal block in the stiffness matrix has size 3×3 and all coefficients are independent for an orthorhombic crystal system [36]. Based on these criteria, both the materials are found to be mechanically stable.

$$\begin{split} &C_{11}>0, \quad C_{11}C_{22}>C_{12}^2, \\ &C_{11}C_{22}C_{33}+2C_{12}C_{13}C_{23}-C_{11}C_{23}^2-C_{22}C_{13}^2-C_{33}C_{12}^2>0 \\ &C_{44}>0, \quad C_{55}>0, \quad C_{66}>0 \end{split} \tag{1}$$

The elastic constants C_{11} , C_{22} and C_{33} determine the linear compressive strength along the $a,\ b$ and c directions [37], respectively. Table 4 shows that the C_{33} value of the BaSnS $_3$ and SrSnS $_3$ compounds is larger than the C_{11} and C_{22} values respectively. As a result, the compounds can be squeezed more along the a and b axes than the c-axis. The elastic constants C_{44} , C_{55} and C_{66} play a crucial role in indirectly influencing a material's hardness. They specifically indicate the materials ability to resist shear deformations along the $(1\ 0\ 0)$, $(0\ 1\ 0)$ and $(0\ 0\ 1)$ planes [38], respectively. Notably, both materials have larger C_{55} values implying that the $(0\ 1\ 0)$ plane is more resistant to shear deformation than the $(1\ 0\ 0)$ and $(0\ 0\ 1)$ planes.

In the elastic region, a solid's properties can be described using four measures: bulk modulus (B), shear modulus (G), Poisson's ratio (ν), and Young's modulus (E). A material's bulk modulus and shear modulus can

be estimated using either the Voigt theory or the Reuss theory. These theories provide upper and lower bounds respectively for the moduli. To obtain a more accurate estimate, the Hill averaging scheme [39] is used to calculate the average of the moduli. The following relations Eqs. (2)–(4) are used to compute the bulk and shear moduli, where B_V , B_R , B_H and G_V , G_R , G_H represent the bulk and shear moduli obtained from Voigt, Reuss and Hill approximations, respectively.

$$B_V = \frac{1}{9} \left[\left(C_{11} + C_{22} + C_{23} \right) + 2 \left(C_{12} + C_{23} + C_{31} \right) \right]$$

$$G_V = \frac{1}{15} \left[\left(C_{11} + C_{22} + C_{33} \right) - \left(C_{12} + C_{23} + C_{31} \right) + 3 \left(C_{44} + C_{55} + C_{66} \right) \right]$$
(2)

$$B_R = \left[\left(S_{11} + S_{22} + S_{33} \right) + 2 \left(S_{12} + S_{23} + S_{31} \right) \right]^{-1}$$

$$G_R = 15 \left[4 \left(S_{11} + S_{22} + S_{33} \right) - \left(S_{12} + S_{23} + S_{31} \right) + 3 \left(S_{44} + S_{55} + S_{66} \right) \right]^{-1}$$
(3)

$$B_H = \frac{B_V + B_R}{2}$$

$$G_H = \frac{G_V + G_R}{2}$$
(4)

The Poisson's ratio (v), Young's modulus (E) and the Vickers hardness (H_V) can be obtained from the bulk and shear moduli by using the

The computed stiffness elastic constants for an orthorhombic XSnS₂ crystal system.

Material	C ₁₁	C ₂₂	C ₃₃	C ₄₄	C ₅₅	C ₆₆	C ₁₂	C ₁₃	C ₂₃
BaSnS ₃	90.145	97.787	109.057	31.774	39.366	31.877	37.177	44.201	35.799
SrSnS ₃	97.256	113.042	119.797	35.971	42.395	36.583	43.866	46.124	34.797

Table 5 Calculated bulk, shear, Poisson's ratio, Young's modulus in GPa and Vickers hardness for BaSnS3 and SrSnS3 materials.

Material	B_{V}	B_R	B_H	G_{V}	G_R	G_H	B_H/G_H	ν	E	H_V	$\mathrm{B_H/C_{44}}$
BaSnS ₃	59.038	58.659	58.849	32.591	31.986	32.288	1.823	0.268	81.891	4.991	1.852
SrSnS ₃	64.408	64.246	64.327	36.677	35.839	36.258	1.774	0.263	91.562	5.734	1.788

following relations: (5)–(7).

$$v = \frac{3B_H - 2G_H}{2(3B_H + G_H)}$$

$$E = \frac{9B_H G_H}{(3B_H + G_H)}$$

$$H_V = \frac{(1 - 2v)E_H}{6(1 + v)}$$
(5)
(6)

$$E = \frac{9B_H G_H}{(3B_H + G_H)} \tag{6}$$

$$H_V = \frac{(1 - 2v)E_H}{6(1 + v)} \tag{7}$$

We can measure the compressibility and deformation resistance to external stress by assessing the bulk and shear moduli. The computed bulk and shear moduli are tabulated in Table 5, and have significant magnitudes. As we can observe, SrSnS3 exhibits large bulk and shear moduli, indicating its ability to withstand linear compressibility and more excellent resistance to deformation under shear stress compared to BaSnS₃. This result is expected, as the bulk modulus is inversely proportional to the cell volume [38]. The computed results are in good agreement with the theory, as SrSnS3 has a smaller cell volume than $BaSnS_3$. Young's modulus (E) describes tensile elasticity. It is a measure of the stiffness of an elastic material and is a quantity used to characterize materials [40]. The calculated E values for BaSnS₃ (81.891 GPa) and SrSnS₃ (91.562 GPa) both indicate noticeable stiffness that is higher than that of Sb₂S₃ and Sb₂Se₃ [41], which are found to be photovoltaic materials [42,43]. Vickers hardness values serve as a measure of a material's resistance to indentation. BaSnS₃ has a Vickers hardness of 4.991, whereas SrSnS₃ exhibits a slightly higher hardness of 5.734, demonstrating that SrSnS₃ has comparatively higher hardness than BaSnS3.

The determination of whether a material is brittle or ductile is significant in a wide range of scientific and material science applications. It is also critical when manufacturing materials with precise mechanical properties. So we employed the Paugh criteria and Poisson's ratio theories to assess whether the material was brittle or ductile. The Pugh criteria [44] involve calculating the ratio of the bulk modulus to the shear modulus of a material $(\frac{B}{G})$. The material is considered ductile if this ratio is greater than 1.75, indicating it can bend and deform without breaking easily. If the ratio is less than 1.75, the material is considered as brittle indicating it is more likely to break or fracture under stress. In our computed results in Table 5, it is clear that both BaSnS3 and SrSnS3 have ratios greater than 1.75 and show ductile nature. The well-known parameter called Poisson's ratio (v) also determines whether the material is brittle or ductile. According to Poisson's ratio, a material is considered ductile if its Poisson's ratio is greater than 0.26, while a ratio less than 0.26 suggests a brittle material. In our computed results, Poisson's ratio for BaSnS₃ (0.268) and SrSnS₃ (0.263) indicates that both materials are ductile. So both theories are consistent and predict a ductile nature for both BaSnS3 and SrSnS₃. The material's ductility can withstand external stress and be used as a photovoltaic absorber material [45]. Poisson's ratio (ν) also describes how the size of a solid varies when forces act perpendicular to its loading direction. In various materials, the thermodynamic limit for the isotropic form of Poisson's ratio is between -1.0 and 0.5. This corresponds to about 0.2 for covalent materials, 0.3 to 0.4 for ionic materials, and 0.5 for pure-ionics [46]. The values for BaSnS₃(0.268) and SrSnS₃ (0.263) indicate that covalent bonding is prominent in both materials.

Computed anisotropic indices for XSnS₂ materials.

Material	\mathbf{A}^U	A_1	A_2	A_3	A_z
BaSnS ₃	0.100	1.147	1.164	1.122	1.199
SrSnS ₃	0.120	1.152	1.038	1.193	1.347

3.2.1. Anisotropy

The degree of elastic anisotropy in a material is measured by the Universal anisotropic factor (A^U) , Shear anisotropic factors $(A_1,$ A_2 , A_3) and Zener anisotropic factor (A_2) . They are determined from Eqs. (8)-(10), respectively. When these factors equal 1, the material is considered perfectly isotropic, while any deviation from this value signifies the degree of elastic anisotropy in the material. The estimated anisotropic factors are presented in Table 6. The computed anisotropy values show that both BaSnS3 and SrSnS3 are elastically anisotropic along three shear planes (0 0 1), (0 1 0) and (1 0 0) which depicts both materials have considerable anisotropy.

$$A^{U} = 5\frac{G_{V}}{G_{R}} + \frac{B_{V}}{B_{R}} - 6 \ge 0 \tag{8}$$

$$A_{1} = \frac{4C_{44}}{C_{11} + C_{22} - 2C_{13}}; A_{2} = \frac{4C_{55}}{C_{22} + C_{33} - 2C_{23}}; A_{3} = \frac{4C_{66}}{C_{11} + C_{22} - 2C_{12}}$$

$$A_z = \frac{2C_{44}}{C_{11} - C_{22}} \tag{10}$$

The ELATE [47] tool was used to create 3D contour plots as well as 2D graphs to visualize crystal elastic anisotropy. These graphical representations illustrate the different moduli, such as Young's modulus (E), shear modulus (G) and Poisson's ratio (ν), enabling a detailed analysis of anisotropy in the crystal structure. The 3D plots can be used to determine the level of anisotropy in solids. A spherical form represents a perfectly isotropic material, and any variation from this sphere reflects the degree of anisotropy present. Figs. 3(a) and 3(d) show the elastic anisotropy of Young's modulus (E) for BaSnS3 and $SrSnS_3$, respectively. These figures exhibit appreciable deviations from a spherical shape, indicating that both the materials exhibit some degree of anisotropy in the Young's modulus. The degree of anisotropy is computed using the E_{max}/E_{min} ratio, resulting in values of 1.439 for BaSnS₃ and 1.484 for SrSnS₃, respectively [48]. We know that atomic arrangements indirectly influence the elastic constants. Materials with stronger atomic bonds tend to exhibit higher elasticity [49]. In our studied materials, distorted octahedra indicate a significant degree of elastic anisotropy taken along different directions. Essentially, the SnS₆ octahedra run along the b-axis (i.e., xz plane), and we have observed a significant anisotropy along the chain direction (xz), as compared to the yz and xy planes, which is further confirmed by the 2D representation presented in supplementary information. Similarly, the anisotropic behavior of the shear modulus and Poisson's ratio is depicted in Figs. 3(b), 3(e) and 3(f) respectively. These figures clearly show that both BaSnS3 and SrSnS3 materials have deviation in spherical form indicates the presence of significant elastic anisotropy.

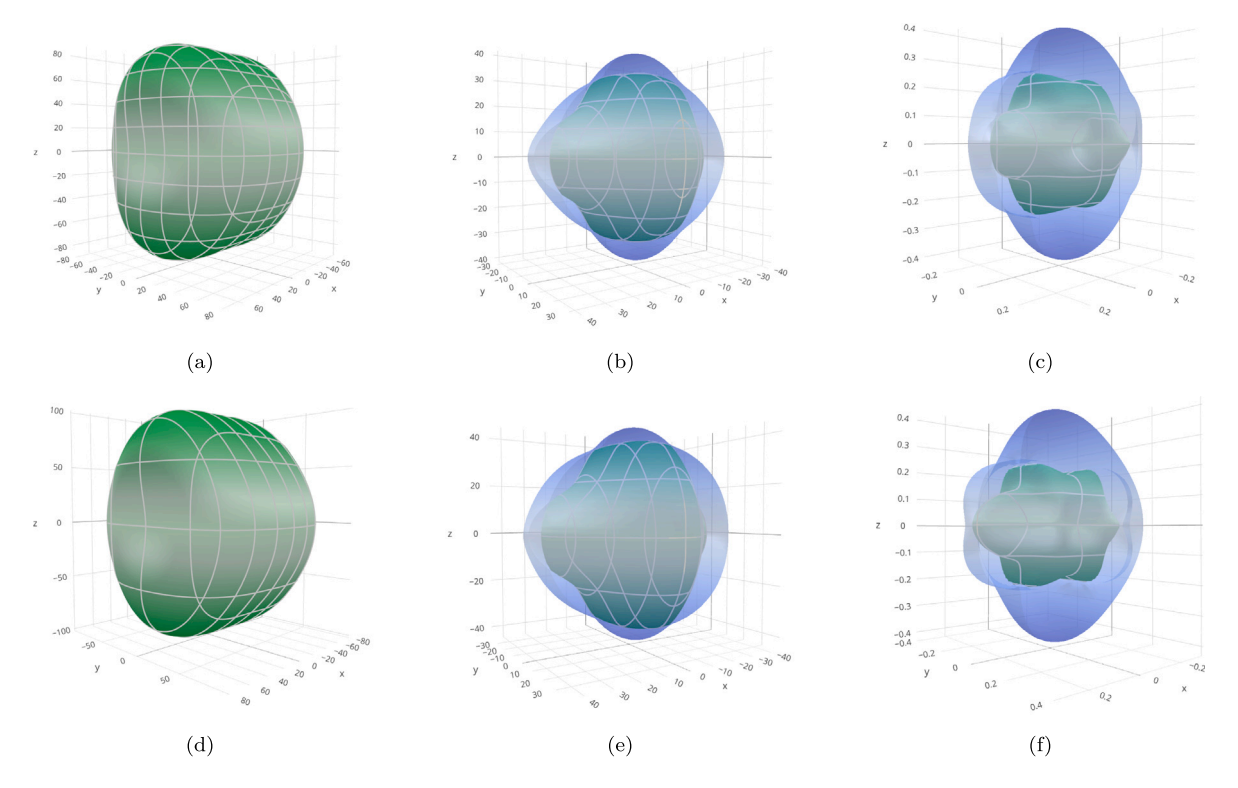


Fig. 3. 3D anisotropic contours representation for BaSnS₃ and SrSnS₃: (a) and (d) Young's modulus, (b) and (e) Shear modulus, (c) and (f) Poisson's ratio, respectively.

The 2D visual representations are presented in supplementary information as Figure S1 and Figure S2 (refer supplementary information) to gain a more comprehensive understanding of directional variations. These illustrations depict the anisotropic behavior of Young's modulus, shear modulus and Poisson's ratio of BaSnS₃ and SrSnS₃ respectively, across the xy, xz, and yz planes. Several observations were made after analyzing these plots. Firstly, Figures S1-a and S2-a show that Young's modulus is more anisotropic in the xz plane compared to the xy and yz planes. It implies a higher degree of anisotropy along the materials *b*-axis (along chain direction). Similarly, we can notice in Figures S1-b, S1-c and Figures S2-b, S2-c that both shear and Poisson's ratios have anisotropy along three directions. We observe that large anisotropy is significant along the xz plane for both BaSnS₃ and SrSnS₃. This result highlights the fact that both the materials possess a quasi-one-dimensional nature along the *b*-axis.

3.3. Electronic properties

The electronic band structures of BaSnS₃ and SrSnS₃ materials have been determined using the optimized lattice parameters. Initially, the GGA-PBE exchange–correlation functional was employed. The results indicate that both materials possess an indirect band gap, with a value of 0.89 for BaSnS₃ and 0.76 for SrSnS₃, respectively. However, several studies suggest that the PBE functional underestimates band gap values [9,22]. To overcome this constraint, we employed the TB-mBJ functional, well-known for providing more precise electronic structure solutions for crystalline systems in solids [50]. To ensure the precision of our computations, we utilized a denser K mesh, consisting of 1000 k-points.

The computed electronic band structures of BaSnS $_3$ and SrSnS $_3$ are shown in Figs. 4(a) and 4(b), respectively. These plots illustrate the band structures at the high-symmetry points of the reciprocal lattice (Γ -X–S-Y- Γ -Z-R-T-U-Z) [51]. The Fermi level E_F , representing zero energy, is indicated by a horizontal straight line. Both BaSnS $_3$ and SrSnS $_3$ materials exhibit moderate bandgap semiconductor characteristics, with measured bandgap values of 1.55 eV and 1.39 eV,

Table 7 Bandgap of $XSnS_3$ (X = Ba, Sr) compounds for different methods.

Material	Method	Bandgap (eV)	Reference
	PBE	0.89	Present work
BaSnS ₃	TB-mBJ	1.55	Present work
	TB-mBJ+SOC	1.55	Present work
	HSE06	1.62	[15]
	PBE	0.76	Present work
SrSnS ₃	TB-mBJ	1.39	Present work
	TB-mBJ+SOC	1.39	Present work
	HSE06	1.40	[15]

respectively. Both possess an indirect band gap nature (Figs. 4(a) and 4(b)). In the case of $BaSnS_3$, the valence band maximum (VBM) is located between the Y- Γ point at coordinates (0.50, 0.00, 0.00), while the conduction band minimum (CBM) is situated between the X–S point at coordinates (0.00, 0.22, 0.00). Similarly, for SrSnS₃, the VBM and CBM are located at coordinates (0.50, 0.00, 0.00) and (0.00, 0.20, 0.00), respectively. The computed band structure values using the TB-mBJ functional are in good agreement with the values reported in previous studies, as listed in Table 7. We have introduced spin–orbit coupling (SOC) in our study to examine its influence on the electronic band gap of the material. Our findings indicate that SOC has a minimal effect on the electronic band gap value, resulting in changes of only a few meV. This result is consistent with previously reported ternary chalcogenide materials [13,52].

We compute the electronic total density of states (TDoS) and projected orbital density of states (PDoS) of the XSnS₃ chalcogenides using the TB-mBJ exchange–correlation functional incorporating SOC to gain profound insights into their electronic structure. Figs. 5(a) and 5(b) illustrate the TDoS and orbital density of states for BaSnS₃ and SrSnS₃, respectively. Fig. 5 illustrates that S atoms dominate the valence band maximum, while Sn and S atoms majorly contribute to the conduction band minimum. The contribution of Ba and Sr atoms is minor in both the conduction and valence bands. The orbital projections into the total

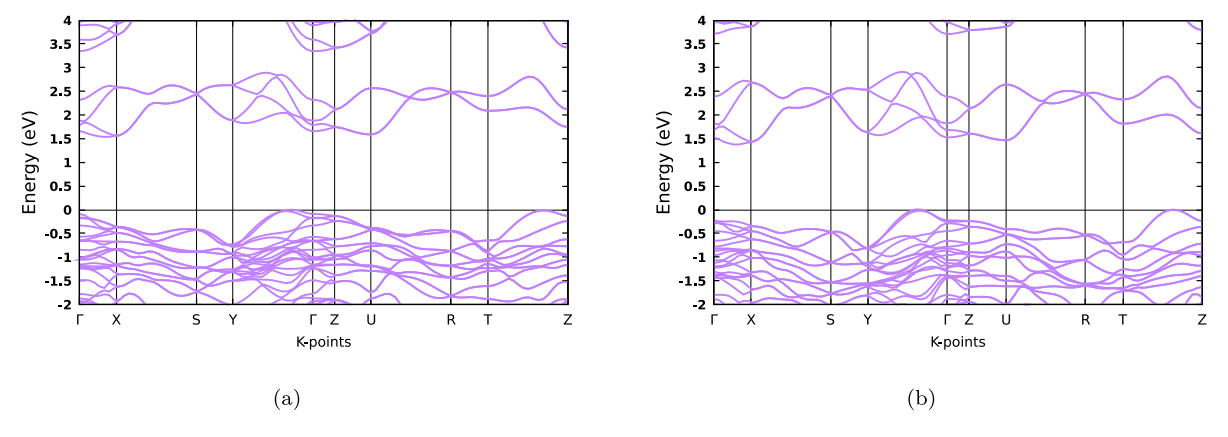


Fig. 4. Band structure of (a) BsSnS3 and (b) SrSnS3 along the high symmetry points.

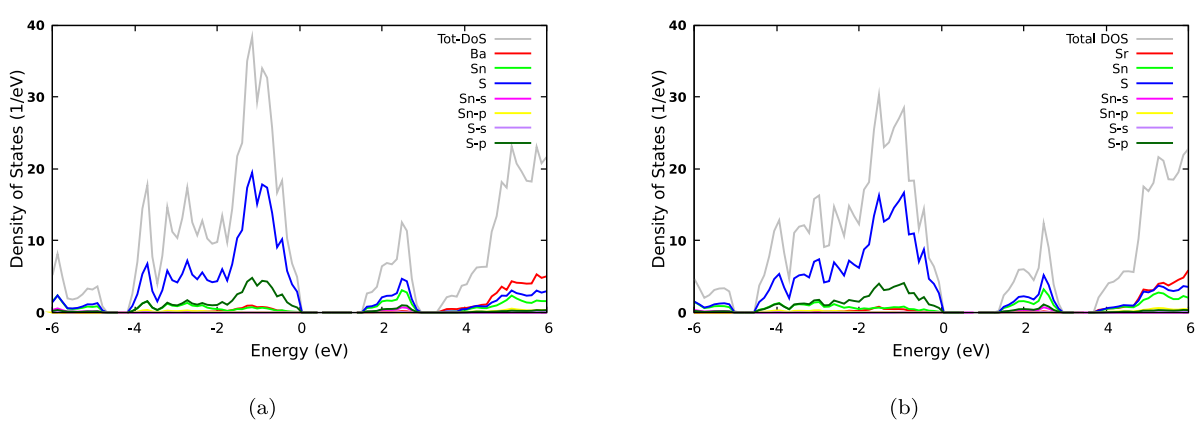


Fig. 5. Total density of states (TDoS) and the projected orbital density of states of (a) BsSnS₃ and (b) SrSnS₃.

density of states provide deeper insights into atomic orbital hybridization. Notably, the S-p orbital and Sn-s orbital hybridization is observed at the conduction band edge. In contrast, the valence band maximum is predominantly influenced by S-p orbital compared to other orbital contributions. A previous report also noted this hybridization between the S-p orbital and Sn-s orbital [15]. Understanding the density of states will aid in tuning the material's band gap.

3.4. Optical properties

Optical transitions involve two distinct mechanism: interband and intraband transitions. Intraband transitions are typically observed in metals or semiconductors that have been heavily doped [53]. Our present work focuses on interband transitions. These transitions occur when electrons within intrinsic semiconductors are energized by photons moving between different electronic bands. The complex dielectric function $\epsilon(\omega)$, a key characteristic in the study of materials optical characteristics [54], is given by Eq. (11). It defines how a material responds to electromagnetic radiation as a function of energy. This study calculates the optical properties by evaluating the complex dielectric function (both real and imaginary parts), refractive index, extinction coefficient, absorption coefficient, birefringence and reflectivity in the photon energy range of 0–10 eV.

$$\epsilon(\omega) = \epsilon^{(1)}(\omega) + i \ \epsilon^{(2)}(\omega)$$
 (11)

Eq. (12) illustrates a direct correlation between a material's electronic structure, interband transitions and optical properties. Here u_k represents the cell periodic Bloch function, q is the incoming radiation wave vector, the parameter Ω corresponds to the volume of the primitive cell, ϵ_k refers to the energy eigenvalues associated with the system, e_a stands for unit vectors along the principal crystal directions and ω_k are

the k-point weights that sum up to 1. By employing the Kramers–Kronig transformation [55], we can derive both the real component $\epsilon^{(1)}$ and the imaginary component $\epsilon^{(2)}$ of the complex parameter ϵ . The interband contribution to the imaginary part of the dielectric functions $\epsilon^{(2)}$ is calculated by summing transitions from occupied (α) to unoccupied (β) states over the Brillouin zone [53]. Considering the spin degeneracy of both the conduction and valence band states, the imaginary part of the dielectric tensor $\epsilon^{(2)}$ is determined using Eq. (12).

$$\epsilon_{\alpha,\beta}^{(2)} = \frac{4\pi^2 e^2}{\Omega} \lim_{q \to 0} \frac{1}{q^2} \sum_{c,v,\mathbf{k}} 2w_{\mathbf{k}} \delta(\epsilon_{c,\mathbf{k}} - \epsilon_{v,\mathbf{k}} - \omega) \times \langle u_{c,\mathbf{k} + e_{\alpha}q} | u_{v,\mathbf{k}} \rangle \langle u_{c,\mathbf{k} + e_{\beta}q} | u_{v,\mathbf{k}} \rangle^*$$
(12)

The real component $\epsilon^{(1)}$ is derived from $\epsilon^{(2)}$ using the Kramers–Kronig transformation [55], as given by Eq. (13).

$$\epsilon_{\alpha,\beta}^{(1)} = 1 + \frac{2}{\pi} P \int_0^\infty \frac{\epsilon_{\alpha,\beta}^{(2)}(\omega')\omega'}{\omega'^2 - \omega^2 + i\eta} d\omega'$$
 (13)

The dispersive real part of the dielectric function $\epsilon^{(1)}(\omega)$ and the absorptive imaginary part $\epsilon^{(2)}(\omega)$ are plotted in Figs. 6(a) and 6(d) for the BaSnS3 and SrSnS3 materials across incident photon energy ranging from 0 to 10 eV. As we observe from Fig. 6(a), the onset value of $\epsilon_0^{(1)}(\omega)$ obtained as 6.22 for BaSnS3 and 6.59 for SrSnS3, which is comparable to those previously reported values for chalcogenide materials utilized in photovoltaic and optoelectronic applications [11,56]. We observe a corresponding rise in the dielectric response as the frequency increases. Notably, these materials demonstrate significantly elevated values of $\epsilon^{(1)}(\omega)$ within the incident photon energy range of up to 5.4 eV, reaching a maximum of 8.84 for BaSnS3 and 8.90 for SrSnS3, respectively. As the energy increases, we can observe a sudden decrease in $\epsilon^{(1)}(\omega)$ reaching zero at 6.46 eV for BaSnS3 and 6.65 eV for SrSnS3. The

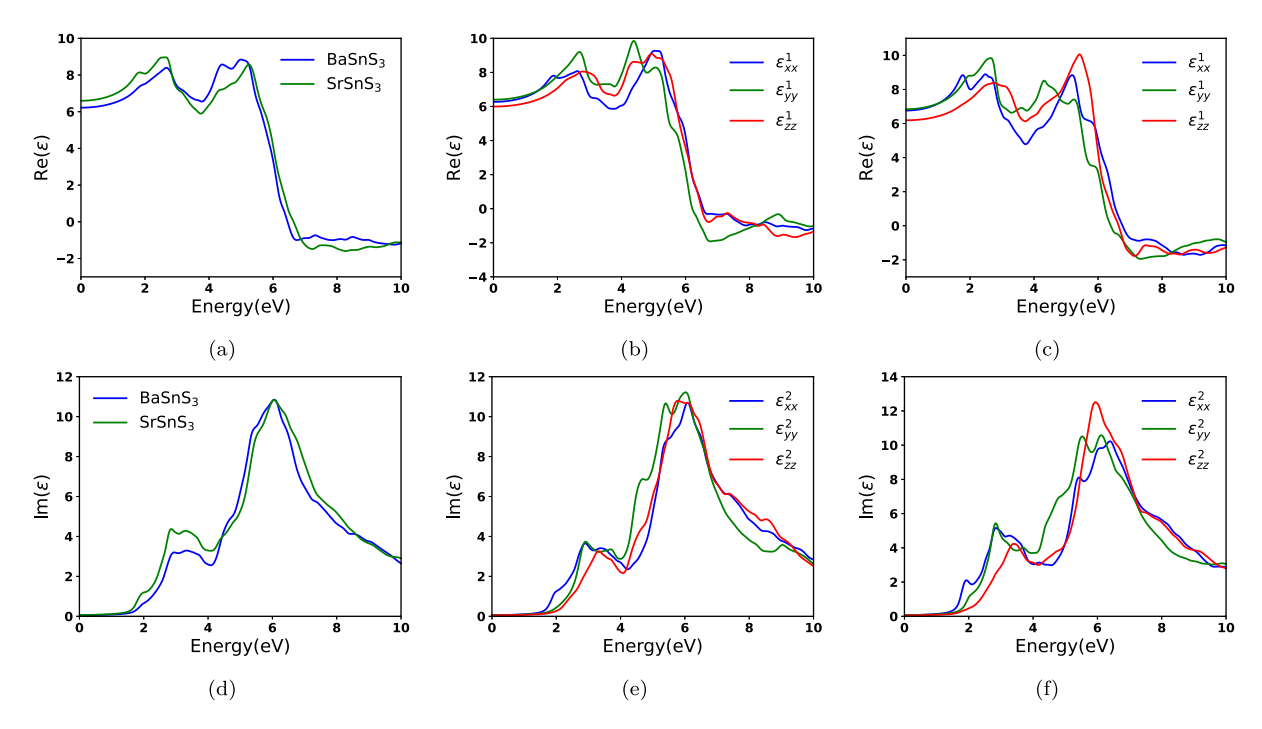


Fig. 6. Dielectric function response plot of XSnS₃ materials: (a) real part $\epsilon^{(1)}$, (d) imaginary part $\epsilon^{(2)}$ variation with energy. Principal components of dielectric function showing the (b) real part $\epsilon^{(1)}$, (e) imaginary part $\epsilon^{(2)}$ for BaSnS₃ and (c) $\epsilon^{(1)}$, (f) $\epsilon^{(2)}$ for SrSnS3, respectively.

negative regions observed after these points are considered to be forbidden regions for electromagnetic wave transmittance [22]. The $\epsilon^{(2)}(\omega)$ component represents the absorptive characteristics corresponding to the material's photon energy. As depicted in Fig. 6(d), it is evident that significant $\epsilon^{(2)}(\omega)$ occurs in the visible to ultraviolet region, ranging from 1.6 to 6.0 eV for BaSnS3 and from 1.42 to 6.0 eV for SrSnS3. The peak values of 10.85 at 6.05 eV and 10.84 at 6.05 eV are observed for BaSnS3 and SrSnS3, respectively. The imaginary part is directly related to the optical bandgap of the materials. Here, we obtain an optical bandgap value of 1.61 eV for BaSnS3 and 1.42 eV for SrSnS3 which is almost similar to the electronic bandgap obtained (See Table 7).

The anisotropic character of the dielectric function is investigated by plotting the values of $\epsilon^{(1)}(\omega)$ and $\epsilon^{(2)}(\omega)$ along distinct crystal directions for both materials, namely. $\epsilon_{xx}^{(1,2)}$, $\epsilon_{yy}^{(1,2)}$ and $\epsilon_{zz}^{(1,2)}$. Figs. 6(b) and 6(c) illustrate the components of the real part dielectric function along different directions for BaSnS3 and SrSnS3, respectively. The onset dielectric constant is larger along the yy direction for both the materials and the data are summarized in Table 8. The anisotropy increases as the energy increases, and the most significant anisotropy occurs for both materials in the incident energy range of 0-5.6 eV. Two peaks are observed: the first in the visible spectrum (2.6–2.8 eV), with the highest values along the yy direction (9.20 for BaSnS3 and 9.85 for SrSnS₃) and the lowest along the zz direction (8.04 for BaSnS₃ and 8.40 for SrSnS₃). The second peak appears around 5 eV in the ultraviolet region, reaching a maximum value of 9.85 for BaSnS₃ (yy direction) and 9.92 for SrSnS₃ (zz direction). Figs. 6(e) and 6(f) depicts the principal components of the imaginary part of the dielectric function. The anisotropy is negligible in the IR region for both the materials; it increases as incident photon energy increases and shows prominent anisotropy in visible and UV region from 1.42-6.0 eV for BaSnS3 and 1.6-6.5 for SrSnS₃ respectively. A material exhibiting a substantial dielectric constant facilitates effective screening and reduces carrier recombination [57,58], suggesting their suitability for photovoltaics and other optoelectronic applications.

The imaginary component of the complex refractive index (the optical extinction coefficient, representing energy loss in the material)

is expressed as Eq. (14),

$$k = \sqrt{\frac{\left[\left(\varepsilon^{(1)}\right)^2 + \left(\varepsilon^{(2)}\right)^2\right]^{1/2} - \varepsilon^{(1)}}{2}}$$
(14)

while its real component (associated with the dispersion of light within the material) is described by Eq. (15).

$$n = \sqrt{\frac{\left[\left(\varepsilon^{(1)}\right)^2 + \left(\varepsilon^{(2)}\right)^2\right]^{1/2} + \varepsilon^{(1)}}{2}}$$
 (15)

The refractive index of the materials at the zero-frequency limit, denoted as the static refractive index n(0), can be computed from Eq. (16) and listed in Table 8.

$$\mathbf{n}(0) = \sqrt{\varepsilon^1(0)} \tag{16}$$

The real part of the complex refractive index along different directions is shown in Figs. 7(a) and 7(c) for BaSnS3 and SrSnS3, respectively. The refractive index (n) increases as the incident energy increases from its static value of 2.49 to 2.75 for BaSnS3 and from 2.57 to 2.89 for SrSnS₃ at 620 nm (2 eV). The refractive indices of both materials are increasing and have two peaks, one in the visible region and the other in the ultraviolet region. The n value attains its maximum value of 3.06 for BaSnS3 and 3.20 for SrSnS3. The refractive indices of both materials are greater than 2.4 in the region of 0-6 eV, and after that, they start decreasing in high-energy region. The decay or reduction in the oscillation amplitude of the incident electric field is associated with the extinction coefficient $k(\omega)$. Figs. 7(b) and 7(d) represent, the anisotropic plot of extinction coefficient for BaSnS₃ and SrSnS₃. $k(\omega)$ exhibits comparable characteristics to the absorption coefficient $\alpha(\omega)$, as they are interconnected through the Beer–Lambert law [59]. Notably, the extinction coefficient remains almost zero in the IR region (Energy < 1.5 eV). It increases with the incident photon energy towards the visible and UV regions. The value of $k(\omega)$ is found to attain its maximum around 6-7 eV and decreases with a further increase in energy due to low absorption. These significant extinction coefficient and refractive index values are comparable to those of several potential solar cell absorber layer materials [60,61].

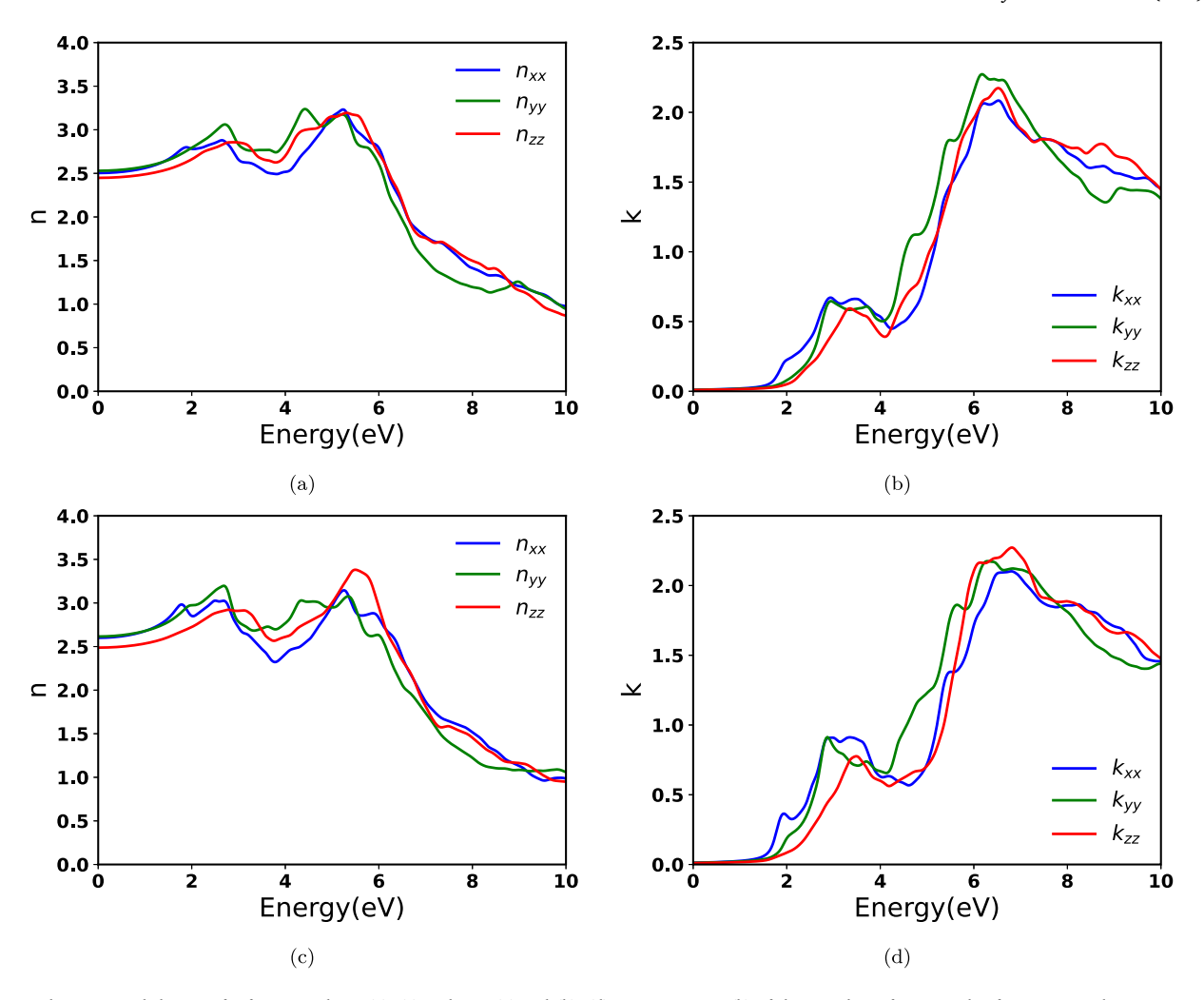


Fig. 7. Optical anisotropy behavior of refractive indices: (a), (c) real part (n) and (b), (d) imaginary part (k) of the complex refractive index for BaSnS₃ and SrSnS₃, respectively.

Table 8 Components of the dielectric function, refractive index and reflectivity of ${\rm XSnS_3}$ compounds.

Dielectric function	$\varepsilon_{xx}^{(1)}(0)$	$\varepsilon_{yy}^{(1)}(0)$	$\varepsilon_{zz}^{(1)}(0)$	$\varepsilon^{(1)}(0)$
BaSnS ₃	6.268	6.398	5.994	6.220
SrSnS ₃	6.761	6.839	6.189	6.596
Refractive index	$n_{xx}(0)$	$n_{yy}(0)$	$n_{zz}(0)$	n(0) (Eq. (16))
BaSnS ₃	2.503	2.529	2.448	2.493
SrSnS ₃	2.600	2.615	2.487	2.568
Reflectivity	$R_{xx}(0)$	$R_{yy}(0)$	$R_{zz}(0)$	
BaSnS ₃	0.184	0.187	0.176	
SrSnS ₃	0.197	0.199	0.181	

Birefringence signifies the variance between the real components of the refractive index across distinct crystal orientations, In contrast, dichroism denotes the difference in the imaginary components of the refractive index along different crystal directions. These are given as:

$$\Delta n = n_i - n_j$$

$$\Delta k = k_i - k_j$$

where i and j represent principal crystal axes, x, y or z (see Fig. 8).

Both materials exhibit uniform birefringence throughout the infrared range, with a value of 0.1 for $BaSnS_3$ and 0.15 for $SrSnS_3$, including short-wave, mid-wave, and long-wave infrared atmospheric transmission regions. Upon further increasing the energy, birefringence

can be observed in both the visible and UV regions, with maximum values of 0.50 for $BaSnS_3$ and 0.53 for $SrSnS_3$, respectively. Similar observations are also found for $HfSnS_3$ and $ZrSnS_3$ materials, which are reportedly suitable for use in photovoltaic cells. The dichroism is found to be isotropic and has a threshold value of 1.6 eV in the infrared region, and is found to be increasing in the visible and UV region with the maximum value of 0.549 for $BaSnS_3$ and 0.551 for $SrSnS_3$ respectively.

The other properties, such as optical absorption coefficient (α) , reflectivity (R) and energy loss function (L) of a material are, determined directly from dielectric function relations Eqs. (17)–(19) respectively.

$$\alpha = \frac{2\omega}{c}k\tag{17}$$

$$R = \frac{[n-1]^2 + k^2}{[n+1]^2 + k^2} \tag{18}$$

$$L = \frac{\epsilon^{(2)}}{(\epsilon^{(1)})^2 + (\epsilon^{(2)})^2} \tag{19}$$

Figs. 9(a)–9(f) represent both material's absorption coefficient, reflectivity, and energy loss function versus energy plots. The absorption coefficients (α) for BaSnS $_3$ and SrSnS $_3$ are shown in Figs. 9(a) and 9(d), respectively. They exhibit a large optical absorption ($\approx 10^6$ cm $^{-1}$) and significant anisotropy in the visible (0.2 × 10 6 cm $^{-1}$) and UV regions. A sharp increase in α is observed around 4 eV for both materials, reaching maximum values of 1.44 for BaSnS $_3$ and 1.50 for SrSnS $_3$, respectively. The substantial absorption coefficient of these materials

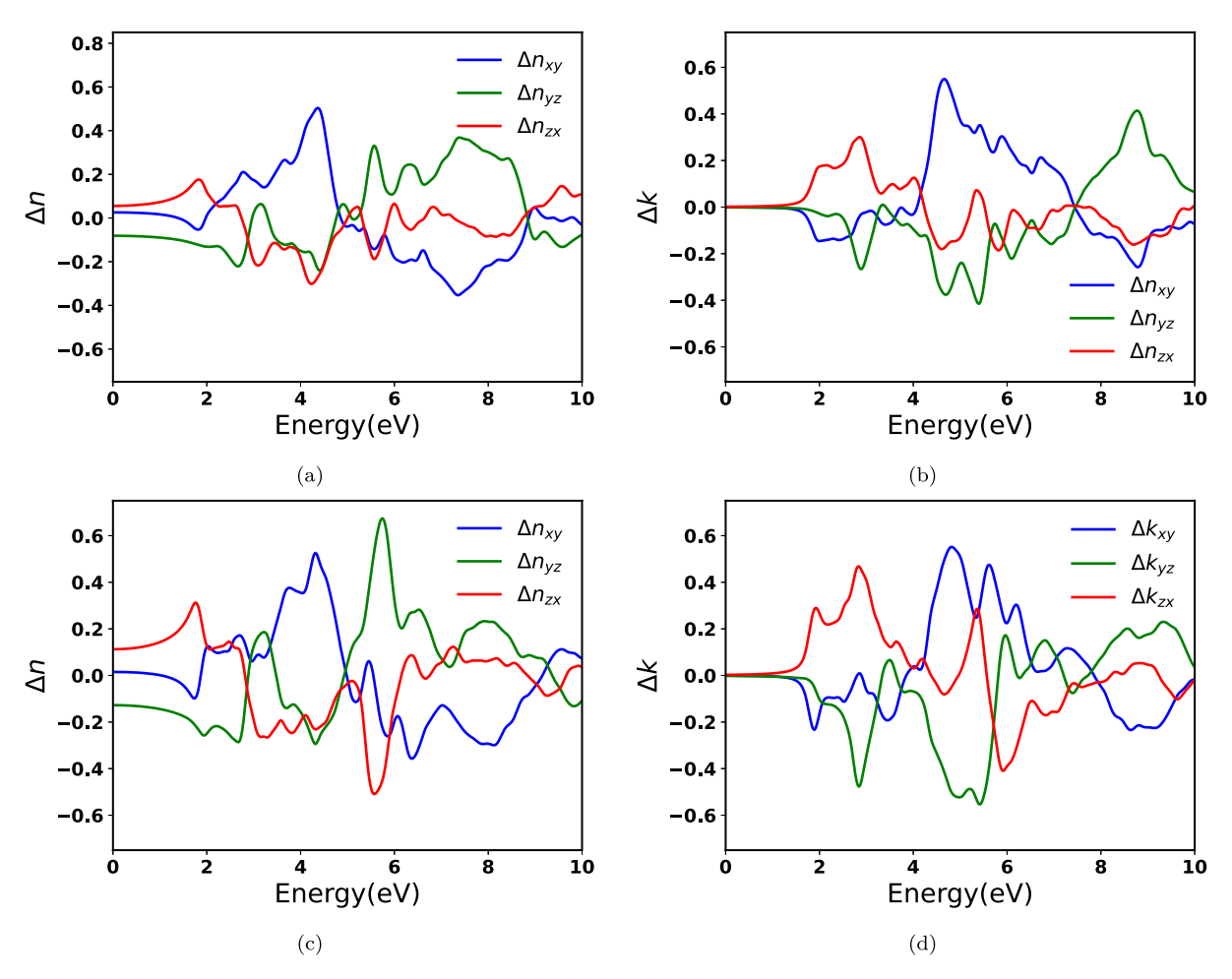


Fig. 8. Frequency dependent birefringence and linear dichroism of XSnS₃ compounds: (a) and (b) for BaSnS₃, and (c) and (d) for SrSnS₃.

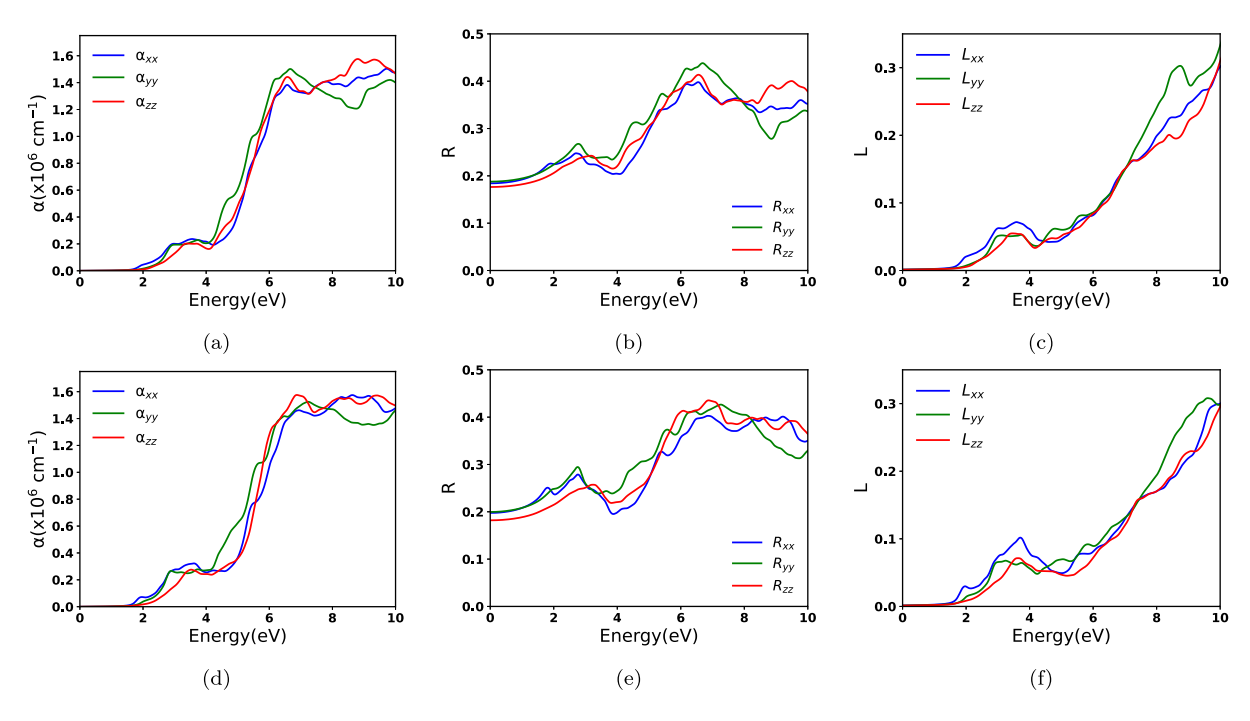


Fig. 9. Optical absorption coefficient (α) of (a) BaSnS₃ and (d) SrSnS₃, reflectivity (R) components along the principal axes for (b) BaSnS₃ and (e) SrSnS₃, and the energy loss function (L) for (c) BaSnS₃ and (f) SrSnS₃.

remains greater than ($\approx 1 \times 10^6$ cm⁻¹) from 4 eV to 10 eV, indicating their potential for use as an absorber material in photovoltaic applications.

The surface characteristics of a material are defined by its reflectivity $R(\omega)$, Figs. 9(b) and 9(e) depicts the reflectivity plots of BaSnS₃ and SrSnS₃, respectively. The average reflectivity of the compounds is reasonably low in the visible region, and it increases with an increase in photon energy, reaching a maximum value of 0.41 (≈40%) at around 6-7 eV, and approximately 0.2 (20%) in the IR and visible regions. The electron energy loss function $L(\omega)$ represents the energy lost by fastmoving electrons as they enter a medium per unit length. Figs. 9(c) and 9(f) depict the anisotropic plots of energy loss function for BasnS₃ and SrSnS3, respectively. Both materials exhibit sustainability with negligible energy loss up to the threshold energy in the IR region, and a further increase in energy will lead to a raise in the energy loss function. They show similar variations and have a value of less than 0.1 in the visible and 0.3 in the UV region. Both material's low reflectivity and energy loss show their applicability in solar cell absorber materials and other optoelectronic applications.

4. Conclusion

Our study focused on the density functional theory analysis of alkaline metal (Ba, Sr) tin chalcogenides XSnS3. The optimized crystal lattices are consistent with the available experimental reports, and both materials are found to crystallize in the orthorhombic space group (Pnma). Notably, the material has a quasi-one-dimensional structure. consisting of edge-shared SnS₆ octahedra that extend along the b-axis. The mechanical stability of the material is determined by the Born stability criteria, computed from the elastic constants Cii. Our findings indicate that both BaSnS3 and SrSnS3 are mechanically stable. The estimated Poisson's ratio and Pugh's ratio indicate that both materials are ductile nature. The anisotropy of the materials is analyzed using the ELATE software. The plots show noticeable anisotropy along the xz plane (along the chain direction) for both BaSnS3 and SrSnS3. Mechanical stability, dutility with significant anisotropy indicate their suitability for material design for opto-electronic applications. Electronic band structure analysis using the TB-mBJ functional reveals that BaSnS₃ (1.55 eV) and SrSnS₃ (1.39 eV) are moderate indirect band gap semiconductors. The obtained band gap values fall within a favorable range for solar cell absorber materials. The projected density of states predicts that the valence band is primarily composed of S-p orbitals, while the hybridized Sn-s and S-p orbital states dominate the conduction band. The analysis of the optical behavior of the studied materials reveals their significant anisotropy, high dielectric constant, and refractive indices. These materials exhibit low energy loss and reflectivity (<40%) across the entire range of incident photon energies from 0 to 10 eV and a high absorption capacity in the visible and ultraviolet regions. The above summarized implications effectively highlight the key findings of the research and the potential applications of the studied materials, particularly emphasizing their suitability for photovoltaic solar cell absorber materials.

Declaration of competing interest

The authors declare that they have no known competing financial interests or personal relationships that could have appeared to influence the work reported in this paper.

Data availability

Data will be made available on request.

Acknowledgments

The author Chethan V. thanks to University Grants Commission (UGC), New Delhi, India for providing financial support (NTA-Ref. No.: 211610131478, Dated: 19-04-2022).

Appendix A. Supplementary data

Supplementary material related to this article can be found online at https://doi.org/10.1016/j.mtcomm.2023.107501.

References

- M. Buffiere, D.S. Dhawale, F. El-Mellouhi, Chalcogenide materials and derivatives for photovoltaic applications, Energy Technol. 7 (11) (2019) 1900819.
- [2] A. Kojima, K. Teshima, Y. Shirai, T. Miyasaka, Organometal halide perovskites as visible-light sensitizers for photovoltaic cells, J. Am. Chem. Soc. 131 (17) (2009) 6050–6051.
- [3] Z. Yi, N.H. Ladi, X. Shai, H. Li, Y. Shen, M. Wang, Will organic-inorganic hybrid halide lead perovskites be eliminated from optoelectronic applications? Nanoscale Adv. 1 (4) (2019) 1276–1289.
- [4] W. Zhang, G.E. Eperon, H.J. Snaith, Metal halide perovskites for energy applications, Nat. Energy 1 (6) (2016) 1–8.
- [5] S. Idrissi, S. Ziti, H. Labrim, L. Bahmad, Band gaps of the solar perovskites photovoltaic CsXCl3 (X=Sn, Pb or Ge), Mater. Sci. Semicond. Process. 122 (2021) 105484
- [6] Y. Selmani, H. Labrim, M. Mouatassime, L. Bahmad, Structural, optoelectronic and thermoelectric properties of Cs-based fluoroperovskites CsMF3 (M=Ge, Sn or Pb), Mater. Sci. Semicond. Process. 152 (2022) 107053.
- [7] A. Babayigit, A. Ethirajan, M. Muller, B. Conings, Toxicity of organometal halide perovskite solar cells, Nat. Mater. 15 (3) (2016) 247–251.
- [8] P. Basera, M. Kumar, S. Saini, S. Bhattacharya, Reducing lead toxicity in the methylammonium lead halide MAPbI 3: Why Sn substitution should be preferred to Pb vacancy for optimum solar cell efficiency, Phys. Rev. B 101 (5) (2020) 054108
- [9] C. Sujith, S. Joseph, T. Mathew, V. Mathew, First-principles investigation of structural, electronic and optical properties of quasi-one-dimensional barium cadmium chalcogenides Ba2CdX3 (X= S, Se, Te) using HSE06 and GGA-PBE functionals, J. Phys. Chem. Solids 161 (2022) 110488.
- [10] C. Sujith, S. Joseph, A. Sneha, T. Mathew, V. Mathew, Large birefringence in the quasi-one-dimensional material Sb2Se3: A DFT investigation of electronic and optical anisotropy, J. Phys. Chem. Solids 174 (2023) 111161.
- [11] C. Sujith, T. Mathew, V. Mathew, Density functional study of electronic and optical properties of quasi-one-dimensional metal tin sulfides MSnS3 (M=Hf, Zr), Solid State Sci. 116 (2021) 106608.
- [12] Y. Lu, W. Yu, Y. Zhang, J. Zhang, C. Chen, Y. Dai, X. Hou, Z. Dong, L. Yang, L. Fang, et al., Synthesis and broadband photodetection of a P-type 1D van der waals semiconductor HfSnS3. Small (2023) 2303903.
- [13] P. Basera, S. Bhattacharya, Chalcogenide perovskites (ABS3; A=Ba, Ca, Sr; B=Hf, Sn): An emerging class of semiconductors for optoelectronics, J. Phys. Chem. Lett. 13 (28) (2022) 6439–6446.
- [14] A.D. Adewoyin, M.A. Olopade, M. Chendo, Prediction and optimization of the performance characteristics of CZTS thin film solar cell using band gap grading, Opt. Quantum Electron. 49 (2017) 1–13.
- [15] Z. Li, H. Xie, Y. Xia, S. Hao, K. Pal, M.G. Kanatzidis, C. Wolverton, X. Tang, Weak-bonding elements lead to high thermoelectric performance in BaSnS3 and SrSnS3: a first-principles study. Chem. Mater. 34 (3) (2022) 1289–1301.
- [16] S. Yamaoka, B. Okai, Preparations of BaSnS3, SrSnS3 and PbSnS3 at high pressure, Mater. Res. Bull. 5 (10) (1970) 789–794.
- [17] B. Okai, K. Takahashi, M. Saeki, J. Yoshimoto, Preparation and crystal structures of some complex sulphides at high pressures, Mater. Res. Bull. 23 (11) (1988) 1575–1584.
- [18] D. Ma, Z. Yang, First-principles studies of Pb doping in graphene: stability, energy gap and spin-orbit splitting, New J. Phys. 13 (12) (2011) 123018.
- [19] M.R. Islam, M.S. Islam, N. Ferdous, K.N. Anindya, A. Hashimoto, Spin-orbit coupling effects on the electronic structure of two-dimensional silicon carbide, J. Comput. Electron. 18 (2019) 407–414.
- [20] M. Mohyedin, M. Taib, A. Radzwan, A. Shaari, M. Mustaffa, B. Haq, M. Yahya, First principles study of the effect of spin-orbit coupling on thermoelectric properties of Bismuth telluride, Comput. Theor. Chem. 1182 (2020) 112851.
- [21] S. Niu, G. Joe, H. Zhao, Y. Zhou, T. Orvis, H. Huyan, J. Salman, K. Mahalingam, B. Urwin, J. Wu, et al., Giant optical anisotropy in a quasi-one-dimensional crystal, Nat. Photonics 12 (7) (2018) 392–396.
- [22] T. Mathew, S. Joseph, V. Mathew, et al., Density functional study of structural, electronic and optical properties of quasi-one-dimensional compounds BaTiX3 (X=S, Se), Superlattices Microstruct. 153 (2021) 106859.
- [23] X. Chen, B. Zhang, F. Zhang, Y. Wang, M. Zhang, Z. Yang, K.R. Poeppelmeier, S. Pan, Designing an excellent deep-ultraviolet birefringent material for light polarization, J. Am. Chem. Soc. 140 (47) (2018) 16311–16319.
- [24] P. Blaha, K. Schwarz, G.K. Madsen, D. Kvasnicka, J. Luitz, et al., wien2k, An augmented plane wave+ local orbitals program for calculating crystal properties 60 (1) (2001).
- [25] P. Blaha, K. Schwarz, F. Tran, R. Laskowski, G.K. Madsen, L.D. Marks, WIEN2k: An APW+ lo program for calculating the properties of solids, J. Chem. Phys. 152 (7) (2020).

- [26] G. Seifert, Tight-binding density functional theory: an approximate Kohn- Sham DFT scheme, J. Phys. Chem. A 111 (26) (2007) 5609–5613.
- [27] J.P. Perdew, K. Burke, M. Ernzerhof, Generalized gradient approximation made simple, Phys. Rev. Lett. 77 (18) (1996) 3865.
- [28] A.D. Becke, E.R. Johnson, A simple effective potential for exchange, J. Chem. Phys. 124 (22) (2006).
- [29] M. Jamal, M. Bilal, I. Ahmad, S. Jalali-Asadabadi, IRelast package, J. Alloys Compd. 735 (2018) 569–579.
- [30] R. Lelieveld, D. Ijdo, Lead zirconium sulphide, Acta Crystallogr. B 34 (11) (1978) 3348–3349.
- [31] G. Wiegers, A. Meerschaut, Misfit layer compounds (MS) nTS2 (M=Sn, Pb, Bi, rare earth metals; T= Nb, Ta, Ti, V, Cr; 1.08< n< 1.23): structures and physical properties, in: Materials Science Forum, Vol. 100, Trans Tech Publ, 1992, pp. 101–172.</p>
- [32] H. Brasseur, L. Pauling, The crystal structure of ammonium cadmium chloride, NH4CdCl3, J. Am. Chem. Soc. 60 (12) (1938) 2886–2890.
- [33] G. Wiegers, A. Meetsma, R. Haange, J. De Boer, Crystal growth, structure and some properties of PbNbS3, SnSNbS3, LaNbS3 and related misfit layer compounds, Solid State Ion. 32 (1989) 183–191.
- [34] Y.-I. Kim, P.M. Woodward, K.Z. Baba-Kishi, C.W. Tai, Characterization of the structural, optical, and dielectric properties of oxynitride perovskites AMO2N (A=Ba, Sr, Ca; M=Ta, Nb), Chem. Mater. 16 (7) (2004) 1267–1276.
- [35] S. Bağcı, M. Cin, H. Uzunok, E. Karaca, H. Tütüncü, G. Srivastava, Investigating the normal state and superconducting state properties of orthorhombic and hexagonal ZrRuP: A first-principles study, Phys. Rev. B 100 (18) (2019) 184507.
- [36] F. Mouhat, F.-X. Coudert, Necessary and sufficient elastic stability conditions in various crystal systems, Phys. Rev. B 90 (22) (2014) 224104.
- [37] T. Özer, Investigation of pressure dependence of mechanical properties of SbSI compound in paraelectric phase by Ab Initio method, Comput. Condens. Matter 28 (2021) e00568.
- [38] A. Khireddine, A. Bouhemadou, S. Alnujaim, N. Guechi, S. Bin-Omran, Y. Al-Douri, R. Khenata, S. Maabed, A. Kushwaha, First-principles predictions of the structural, electronic, optical and elastic properties of the zintl-phases AE3GaAs3 (AE=Sr. Ba). Solid State Sci. 114 (2021) 106563.
- [39] R. Hill, The elastic behaviour of a crystalline aggregate, Proc. Phys. Soc. A 65 (5) (1952) 349.
- [40] Q. Fan, C. Chai, Q. Wei, Y. Yang, Two novel silicon phases with direct band gaps, Phys. Chem. Chem. Phys. 18 (18) (2016) 12905–12913.
- [41] H. Koç, A.M. Mamedov, E. Deligoz, H. Ozisik, First principles prediction of the elastic, electronic, and optical properties of Sb2S3 and Sb2Se3 compounds, Solid State Sci. 14 (8) (2012) 1211–1220.
- [42] R. Kondrotas, C. Chen, J. Tang, Sb2s3 solar cells, Joule 2 (5) (2018) 857-878.
- [43] M. Delaney, I. Zeimpekis, D. Lawson, D.W. Hewak, O.L. Muskens, A new family of ultralow loss reversible phase-change materials for photonic integrated circuits: Sb2S3 and Sb2Se3, Adv. Funct. Mater. 30 (36) (2020) 2002447.

- [44] S. Pugh, XcII. Relations between the elastic moduli and the plastic properties of polycrystalline pure metals, Lond., Edinb., Dublin Philos. Mag. J. Sci. 45 (367) (1954) 823–843.
- [45] J. Feng, Mechanical properties of hybrid organic-inorganic CH3NH3BX3 (B=Sn, Pb; X=Br, I) perovskites for solar cell absorbers, Apl Mater. 2 (8) (2014).
- [46] S. Saha, G. Dutta, Elastic and thermal properties of the layered thermoelectrics BiOCuSe and LaOCuSe, Phys. Rev. B 94 (12) (2016) 125209.
- [47] R. Gaillac, P. Pullumbi, F.-X. Coudert, ELATE: an open-source online application for analysis and visualization of elastic tensors, J. Phys.: Condens. Matter 28 (27) (2016) 275201.
- [48] E. Tindibale, W.M. Mulwa, B.I. Adetunji, Elastic, anisotropic, lattice dynamics and electronic properties of XNiM and XNi2M (X=Ti, Zr, Hf; M=Sn, Ge, Si): DFT comparison study, Physica B 665 (2023) 415029.
- [49] K. Panda, K.R. Chandran, First principles determination of elastic constants and chemical bonding of titanium boride (TiB) on the basis of density functional theory, Acta Mater. 54 (6) (2006) 1641–1657.
- [50] G. Rehman, M. Shafiq, Saifullah, R. Ahmad, S. Jalali-Asadabadi, M. Maqbool, I. Khan, H. Rahnamaye-Aliabad, I. Ahmad, Electronic band structures of the highly desirable III–V semiconductors: TB-mBJ DFT studies, J. Electron. Mater. 45 (2016) 3314–3323.
- [51] W. Setyawan, S. Curtarolo, High-throughput electronic band structure calculations: Challenges and tools, Comput. Mater. Sci. 49 (2) (2010) 299–312.
- [52] C. Sujith, S. Joseph, T. Mathew, V. Mathew, Large optical anisotropy in quasi-one-dimensional tantalum thallium chalcogenides TaTlX3 (X=S, Se): A first-principles investigation, Mater. Chem. Phys. 303 (2023) 127754.
- [53] M.S. Yaseen, J. Sun, H. Fang, G. Murtaza, D.S. Sholl, First-principles study of electronic and optical properties of ternary compounds AuBX2 (X=S, Se, Te) and AuMTe2 (M=Al, In, Ga), Solid State Sci. 111 (2021) 106508.
- [54] A. Forouhi, I. Bloomer, Optical properties of crystalline semiconductors and dielectrics, Phys. Rev. B 38 (3) (1988) 1865.
- [55] C. Ambrosch-Draxl, J.O. Sofo, Linear optical properties of solids within the full-potential linearized augmented planewave method, Comput. Phys. Commun. 175 (1) (2006) 1–14.
- [56] M. Suhail, H. Abbas, M.B. Khan, Z.H. Khan, Chalcogenide perovskites for photovoltaic applications: a review, J. Nanoparticle Res. 24 (7) (2022) 142.
- [57] R.H. Bube, Photoelectronic Properties of Semiconductors, Cambridge University Press, 1992.
- [58] C. Persson, Electronic and optical properties of Cu2ZnSnS4 and Cu2ZnSnSe4, J. Appl. Phys. 107 (5) (2010).
- [59] D.F. Swinehart, The beer-lambert law, J. Chem. Educ. 39 (7) (1962) 333.
- [60] P. Hlidek, J. Bok, J. Franc, R. Grill, Refractive index of CdTe: Spectral and temperature dependence, J. Appl. Phys. 90 (3) (2001) 1672–1674.
- [61] W. Primak, Refractive index of silicon, Appl. Opt. 10 (4) (1971) 759-763.